VIII International Conference on Textile Composites and Inflatable Structures
STRUCTURAL MEMBRANES 2017
K.-U.Bletzinger, E. Oñate and B. Kröplin (Eds)

THE EFFECT OF GRAVITY IN TRANSIENT FLUID-STRUCTURE INTERACTION SIMULATIONS OF A LARGE WIND TURBINE WITH COMPOSITE BLADES

G. SANTO[*], M. PEETERS[†], W. VAN PAEPEGEM[†] AND J. DEGROOTE[*]

[*] Department of Flow, Heat and Combustion Mechanics, Ghent University
Sint-Pietersnieuwstraat 41 – 9000 Ghent, Belgium
{gilberto.santo; joris.degroote}@ugent.be

[†] Department of Materials, Textiles and Chemical Engineering, Ghent University
Technologiepark-Zwijnaarde 907 – 9052 Zwijnaarde, Belgium
{mathijs.peeters; wim.vanpaepegem}@ugent.be

Key words: Fluid-Structure Interaction, Composite Materials, Wind Turbine, Atmospheric Boundary Layer.

Summary. In this work the effect of the gravity force on the fluid-structure interaction (FSI) simulation of a large horizontal axis wind turbine (HAWT) is analyzed in detail. FSI simulations with and without gravity are carried out and compared in order to highlight the effect of gravity force on the loads and performance of the analyzed HAWT.

1 INTRODUCTION

The increasing size of the horizontal axis wind turbine's rotor[1] in order to maximize the captured energy, and the resulting higher slenderness of their blades, have led to the need of investigating the mutual interaction of wind flow and structural response of the blades. It has already been shown in previous research that the axial deflection of the blade tips can reach 10-15% of the total blade span during the normal operation of wind turbines[2, 3]. The deforming motion of the blades influences the wind flow around them and, in turn, the wind loads are also modified. This results in a fully coupled fluid-structure interaction (FSI) problem, which is important to be accounted for in many processes such as design and maintenance estimation of modern horizontal axis wind turbines (HAWTs) [4].

Both the aerodynamic and the structural sides of the FSI problem involve a large number of complexities when it comes to numerical simulation. On the aerodynamic side, the high Reynolds number of the flow (up to 10^8) and the consequent high turbulence levels are challenging to simulate. Furthermore, wind turbines are immersed in the atmospheric boundary layer (ABL) [5, 6], i.e. an increasing wind speed with height, such that the complete rotor has to be simulated with the loads on each blade fluctuating in time. On the structural side, HAWT blades are normally made of anisotropic composite materials built up of several plies[7, 8]. The presence of inner structures (shear webs and shear caps) and adhesive joints makes the modelling even more challenging. The gravity load also plays a major role on the structural response of the blades and will be the focus of this paper.

The present work aims at simulating the fully coupled FSI problem on a full scale HAWT employing accurate flow and structural models, leading to a fully coupled FSI model. The ABL is taken into account in detail as opposed to what is normally done in literature. The gravity load is considered in the structural model and its effect is highlighted by comparison with analogous results obtained neglecting this load. The oscillating loads and stresses on each blade are analysed in detail. On the structural side, a complete and accurate model reproducing the complex composite nature of each blade is built and employed. The implicit coupling between the flow and the structural models is guaranteed by the in-house code Tango, resulting in a segregated approach[9].

2 METHODOLOGY

Both the computational fluid dynamics (CFD) and computational structural mechanics (CSM) models are now described. Afterwards, the details of the coupling will be given.

2.1 The CFD model

In terms of modelling, the inclusion of the ABL implies that the entire rotor needs to be analyzed and the reduction to one single blade with periodic boundary conditions is not possible. Furthermore, different reference frames are necessary: a stationary and a rotating domain are adopted. The layout of the complete mesh is shown in fig. 1.

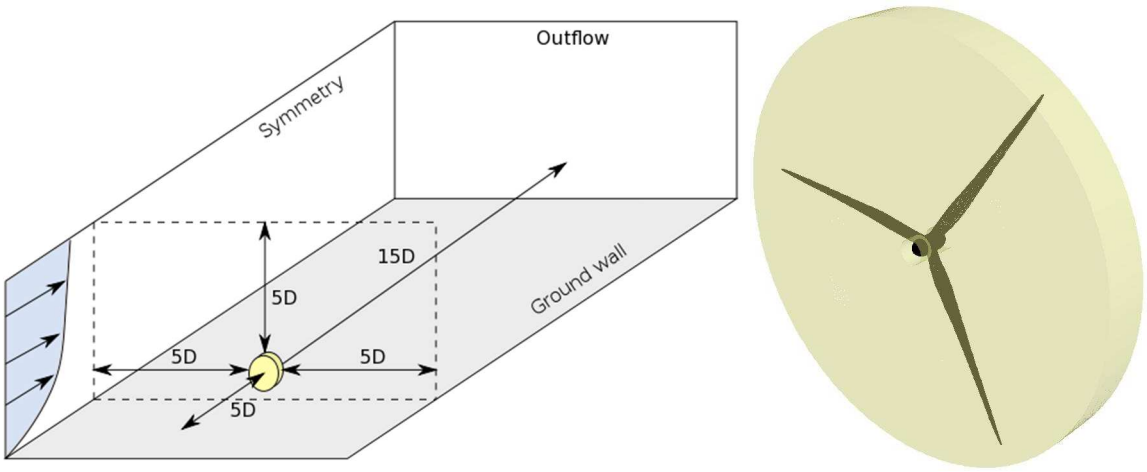

Figure 1: (left) layout of the HAWT simulations and (right) detail of the rotating domain.

The rotor, whose radius R is 50m, is embedded in the rotating cylindrically-shaped domain (marked in yellow in fig. 1), which has a length of 12 m and a radius of 52 m. The rotating and stationary domains are separated by sliding interfaces where all the information is passed through by interpolation. The distance of the rotor from the symmetry sides and top surface is chosen equal to 5 rotor diameters in order to avoid artificial acceleration of the flow. The inflow and the outflow are respectively 5 and 15 rotor diameters away from the rotor. These distances

are chosen sufficiently large to avoid any influence of the boundaries on the flow around the turbine.

The case is considered to be incompressible, given the low Mach numbers typical of the HAWTs. The turbulence model is chosen to be the *k-epsilon* (unsteady RANS) model. The ABL inlet conditions first proposed by Richard and Hoxey[5] are employed for the velocity u, the turbulent kinetic energy k and the dissipation rate ε in order to replicate the neutral ABL (no heat flux) conditions in the numerical domain, with z the height, thus the distance from the ground wall.

$$u(z) = \frac{u_*}{\mathrm{K}} ln\left(\frac{z + z_0}{z_0}\right)$$

$$k = \frac{u_*^2}{\sqrt{C_\mu}}$$

$$\varepsilon(z) = \frac{u_*^3}{\mathrm{K}(z + z_0)}$$

In these equations, u_* is the friction velocity, an index of the global wind intensity, and z_0 is the aerodynamic roughness length which provides a measure of how rough the ground wall is. These two parameters fully define the ABL characteristics. K is the von Karman constant (0.4187) while C_μ is a constant of the *k-epsilon* model (0.09).

To guarantee that the profiles imposed as inlet conditions are preserved throughout an empty domain, a new formulation of the wall functions for the ground wall is required. Thus, the aerodynamic roughness length is explicitly included in the wall functions, following the formulation proposed by Parente et al. [6], leading to a modified non-dimensional wall distance z^+ and a modified wall function constant E.

$$z_{mod}^+ = \frac{(z + z_0)u_*\rho}{\mu}$$

$$E_{mod} = \frac{\mu}{\rho z_0 u_*}$$

On the inlet surface, the previously defined inlet ABL profiles are prescribed with u_*= 0.791959 m/s and z_0= 0.5 m. The standard wall functions are employed on the rotor walls, while the modified ones are employed on the ground wall. The mesh is fully structured and composed of 13M cells in total, 3M for the rotating domain and 10M for the stationary one. The mesh in the rotating domain (highlighted in yellow in fig. 1) is obtained by means of a multi-block strategy. Only one blade and the 120° sector around it are explicitly meshed, while the complete rotor mesh is obtained taking advantage of the geometrical periodic condition, thus repeating the one sector mesh two more times. Two sections of the mesh around one single blade are shown in fig. 2, with one of them taken close to the blade root and the other close to the blade tip.

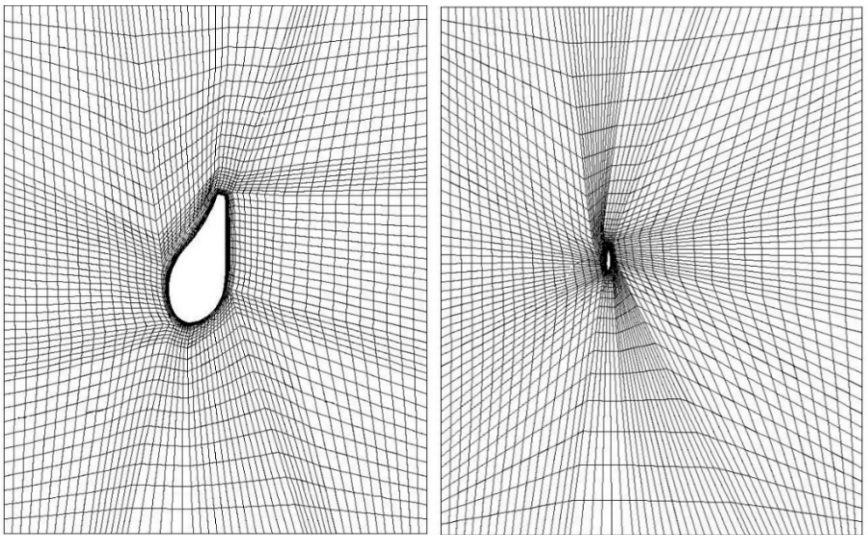

Fig. 2 – Sections of the mesh around one blade: (left) close to the root at r/R = 20% and (right) close to the tip at r/R = 99%.

The momentum equations and pressure-based continuity equation are solved together with implicit coupling. 2nd order upwind discretization for momentum is applied and a 2nd order implicit scheme is used for time discretization.

2.2 The CSM model

The analyzed blade is entirely made of composite material, with a total weight exceeding 9 tons. Several airfoils are lofted throughout its 50 m span. Inside the structure itself, three shear webs cover a large portion of the total span and provide additional stiffness to the blade.

Only shell elements with reduced integration are employed and composite layups are defined to reproduce the composite layering. The elements are positioned on the outer mold layer (OML) with material offset towards the inside, mimicking the blade's manufacturing process and maintaining the correct outer blade shape. Different layups are assigned to different regions of the structure, modelling its real composition. A local reference frame is discretely defined in every element in order to fix the global orientation of the layup. Every layup is then composed of a varying number of plies ranging from 1 to 127. For each ply, a material and a thickness are assigned, together with a relative orientation in the form of a rotation angle with respect to the global layup orientation. This relative orientation is necessary to fully define the characteristics of layers made of anisotropic materials. In every element, the stresses are computed in each ply. The shear webs and the shear caps are modelled using the same strategy. The adhesive joints are also included in the model by the introduction of layers of adhesive material. The mesh is created according to the process outlined and discussed in ref.[7]. Following this procedure, a mesh composed of 64000 three-dimensional shell elements is obtained, as shown in fig. 3.

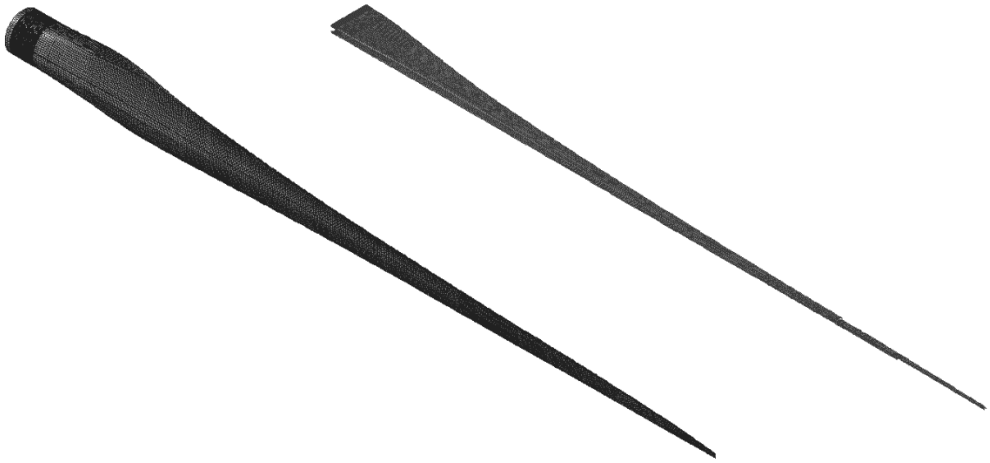

Figure 3: (left) overview of the structural mesh and (right) inner structures.

In order to validate the structural model, the eigenfrequencies of the blade are computed, pinning its root. The manufacturer provides only ranges for the first flap-wise and chord-wise modes as benchmarks. The results of the modal analysis are reported in Table 1.

Table 1: Experimental/numerical comparison of the eigenfrequencies of the blade.

	Manufacturer	Modal analysis
First flap-wise mode	0.74 Hz – 0.91 Hz	0.644 Hz
First chord-wise mode	1.01 Hz – 1.35 Hz	1.162 Hz

In the FSI simulations, the rotational speed is fixed at the root of the blade, where any other degree of freedom is constrained.

Two distinct dynamic simulations are carried out and analyzed. The coupled simulation with no gravity in the structural model will be, in the remainder, addressed as "FSI". In contrast with it, the simulation where the gravity force is accounted for on the blade structures will be called "FSIg". The results of these two cases will be compared in order to clearly highlight the effect of the gravity load on the blade operation.

2.2 FSI coupling

The CFD and CSM models are coupled by an in-house code, named Tango[9]. Within every time step, the information is exchanged as outlined in fig. 4.

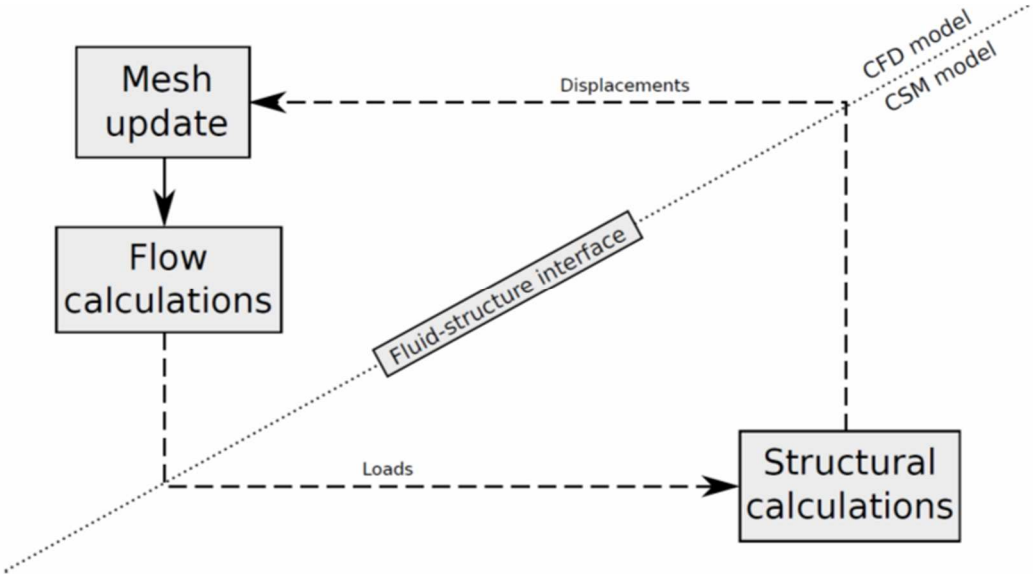

Figure 4: FSI coupling scheme (Gauss-Seidel).

This strategy corresponds to the Gauss-Seidel coupling algorithm. Given the non-conformal meshes, interpolation is required when any information (loads or displacements) is passed from one side of the fluid-structure interface to the other. A 2nd order spatial interpolation is therefore applied in both directions.

The displacements are applied on the blades according to the output of the structural solver at the beginning of every coupling iteration. In the first coupling iteration of every time step, no mesh update in addition to rigid rotation is performed since there is still no structural data available for the current time step. An arbitrary Lagrangian Eulerian (ALE) formulation is employed for the mesh update. Only the mesh in the rotating domain is deformed by means of the diffusion method with diffusivity based on boundary distance. Once the deformation of the blades is read in, the mesh velocity $\vec{w}$ in the rotating domain is obtained by solving the equation $\nabla \cdot (\gamma \nabla \vec{w}) = 0$ with d the distance from the blade wall and with the diffusivity γ defined as $\gamma = 1/d^a$. The diffusion factor a is chosen to be 1 in the case without gravity and 1.2 in the case with gravity. The boundary conditions for the diffusion equation are the prescribed motion of the blades and the need to preserve the shape of the sliding interfaces.

In this work, the rotational speed of the turbine is chosen to be 1.3 rad/s. Combined with a wind speed of 10 m/s (at the hub height), this leads to a tip speed ratio λ approximately equal to 6.5. 120 time steps are required to complete a full revolution. The loop shown in fig. 4 is repeated 3 times within every time step, leading to fluid-structure interface displacement absolute residual to drop below 5 cm.

3 RESULTS AND DISCUSSION

In this section, the results of the FSI and FSIg calculations will be presented. Both the simulations are transient and are started from the results of a steady state one. In the remainder, the logics illustrated in fig. 5 will be followed when defining the azimuth angle of each blade

and the sign of the radial and tangential forces and velocities.

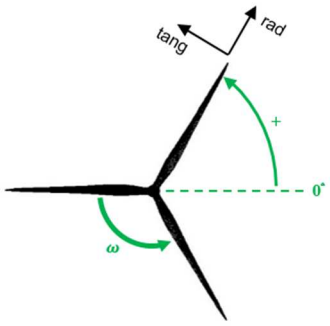

Figure 5: Definitions of blade azimuth angle and components of forces and velocities.

Furthermore, the torque T acting on the blades is made non-dimensional by means of the following formula:

$$c_T = \frac{T}{\frac{1}{2}\rho v^2 AR}$$

where ρ is the air density, A the frontal area of the rotor and R its radius. The velocity v of the undisturbed flow is chosen to be the wind free stream velocity at the hub height, namely 10 m/s. Starting from a steady FSI simulation, one full revolution of the rotor is necessary to reach regime in time. Fig. 6 illustrates the contours of velocity magnitude in a section of the computational domain, showing the velocity distribution typical of the neutral ABL.

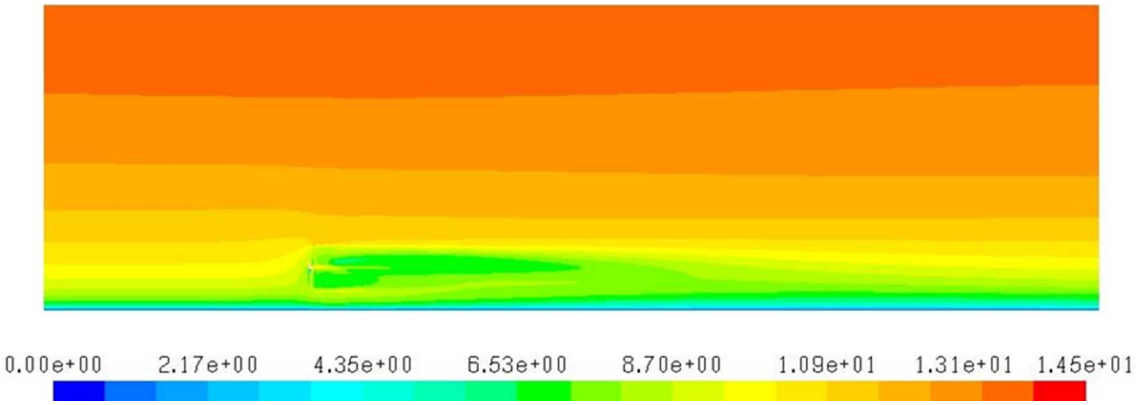

Figure 6: contours of velocity magnitude [m/s] across the computational domain.

For an azimuth angle between 0 and 180 *deg* (i.e. when the blade points upwards), the wind velocity is higher, leading to higher angle of attacks and higher relative incoming velocity throughout the entire blade span (fig. 7).

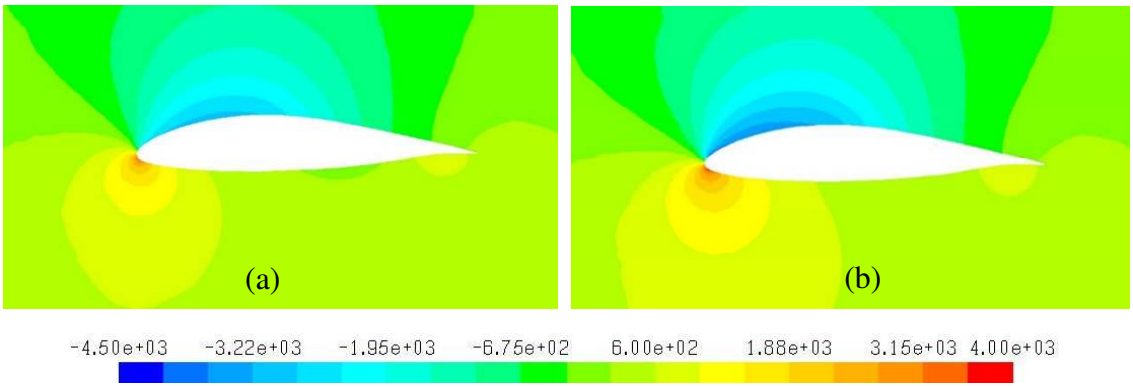

Figure 7: Pressure contours [Pa] around blade tip section at azimuth angles of (a) -90˚ and (b) +90˚.

As a direct consequence, also the bending moment on the blade varies. Additionally, the gravity force tends to increase the bending moment when the blade point upwards, while it tends to decrease it when the blade point downwards, as illustrated by fig. 8.

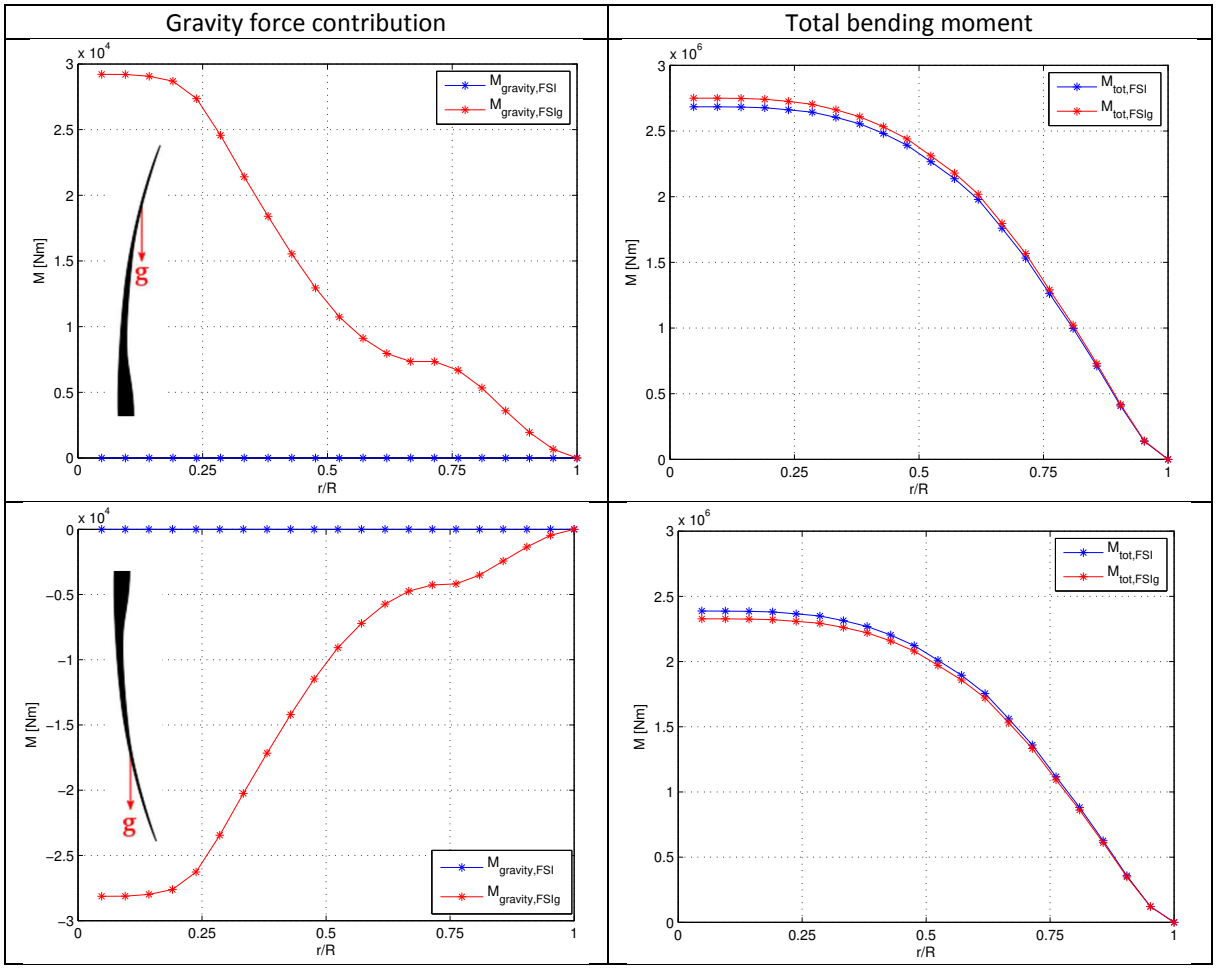

Figure 8: Flapwise bending moment diagrams: bending moment as a function of the radial position along the blade for azimuth angles of (up) +90˚ (blade vertically up) and (down) -90˚ (blade vertically down).

The varying gravity contribution to the bending moment translates directly into an increased amplitude of the tip axial displacement oscillation in the FSIg case with respect to the FSI case. Fig. 10 compares the tip axial displacement and the tip axial velocity in both cases.

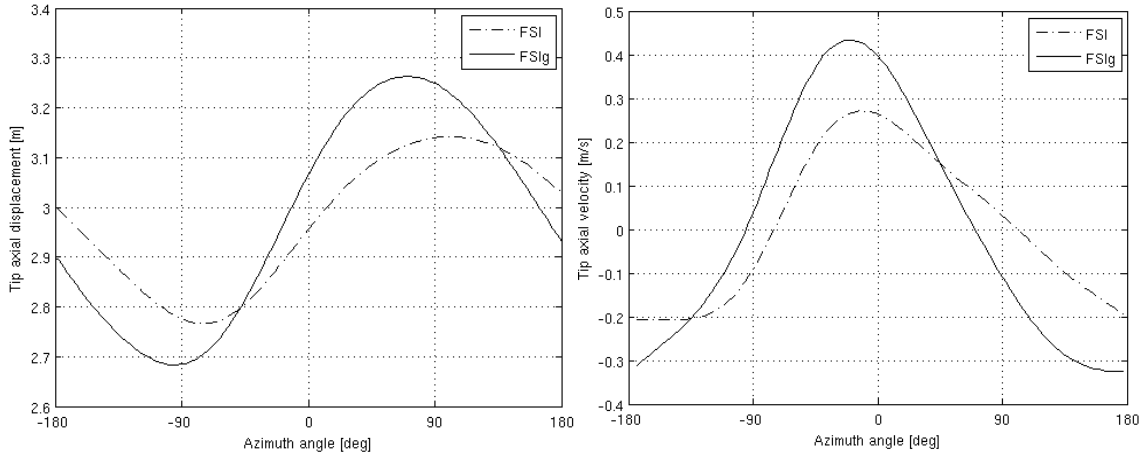

Figure 10: (left) Tip axial displacement and (right) tip axial velocity.

Similarly, also the tip tangential displacement and the consequent tangential velocity are sensibly affected by the gravity force, as shown by fig. 11.

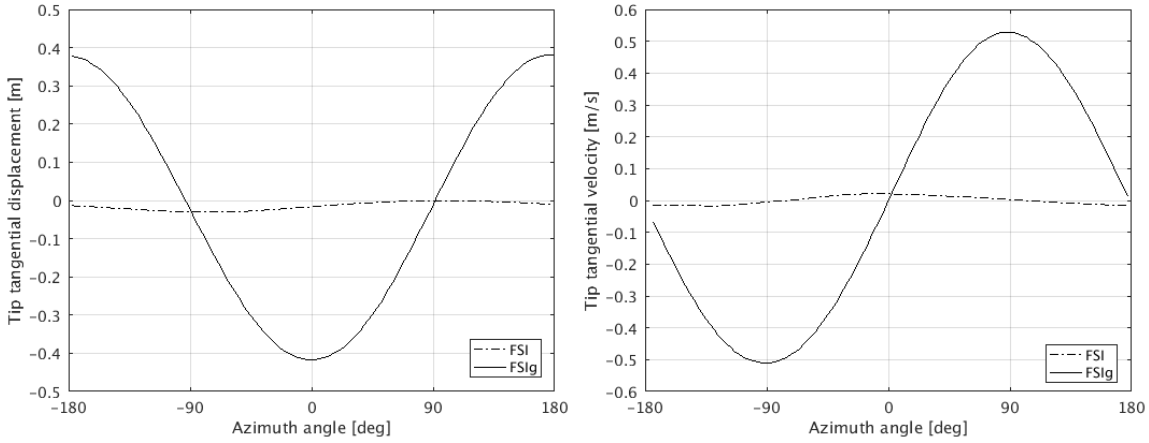

Figure 11: (left) Tip tangential displacement and (right) tip tangential velocity.

The gravity tends to tangentially deflect the blade when it is horizontally positioned, namely for 0 and $\pm 180\ deg$ azimuth angles. The blade deflection will also modify the blade speed, modifying the velocity triangles throughout the revolution.

Despite the constancy of the total torque coefficient (0.0291 for both FSI and FSIg), the single blade contribution varies throughout the revolution as shown in fig. 12. The oscillation of the torque provided by each blade is a direct consequence of the velocity gradient induced by the ABL.

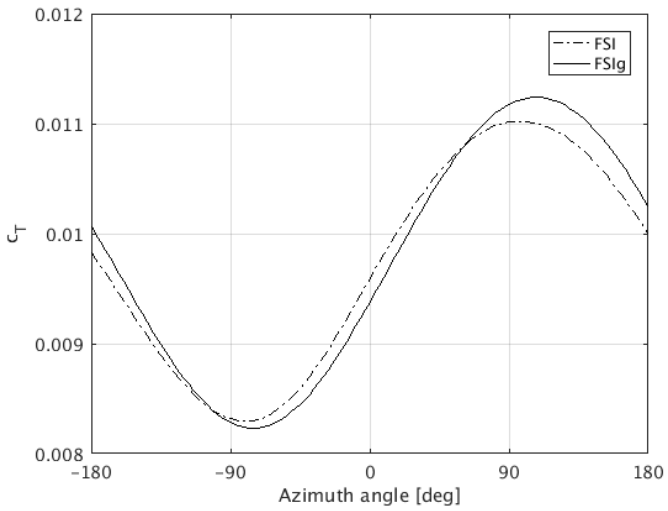

Figure 12: Single blade contribution to the torque.

Moreover, a delay in the peak of the torque contribution of each blade is observed in the FSIg case with respect to the FSI case. This difference is linked to the different magnitude and direction of the tip velocity. When the blade tip undergoes a negative axial velocity (i.e. displaces towards the incoming flow and its displacement decreases in magnitude) a beneficial effect is expected on the blade tip performance: the apparent wind speed (purely axial) is increased by the negative axial velocity of the tip, which leads to higher angles of attack and higher relative velocity magnitude. On the other hand, the same reasoning can be reversed for positive tip axial velocity. Similarly, an increase in the tip tangential speed leads on the one hand to an increase in the relative velocity magnitude, but on the other hand to a decrease in the angle of attack. The two effects counteract each other and it is not straightforward to assess which one dominates on the other during the blade motion. The blade axial and tangential velocities can be used to correct the blade speed and reconstruct the evolution of the angle of attack at the tip of the blade. Fig. 13 shows the difference in the tip angle of attack between FSIg and FSI case and compares it with the difference in torque between the same cases.

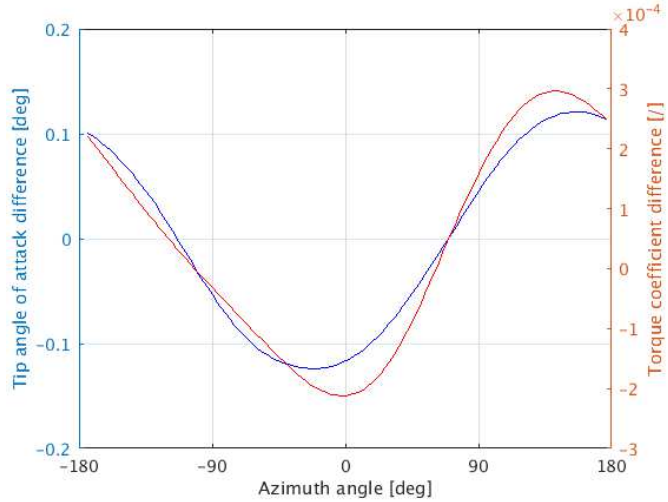

Figure 13: Tip angle of attack difference and torque coefficient difference between FSIg and FSI cases.

The qualitative similarity of these two differences is a strong indication that the tip velocity induced by its deflection has an effect on the local angle of attack and thus on the local performance of the blade and this effect can be seen in the torque coefficient evolution as well.

In terms of internal stresses, the inner structures (shear webs) of the blade are responsible for most of its structural response. Fig. 14 shows the pattern of the bending solicitation acting on them. Furthermore, fig. 15 shows the magnitude of the maximum (traction) and minimum (compression) stress in the blade shear webs.

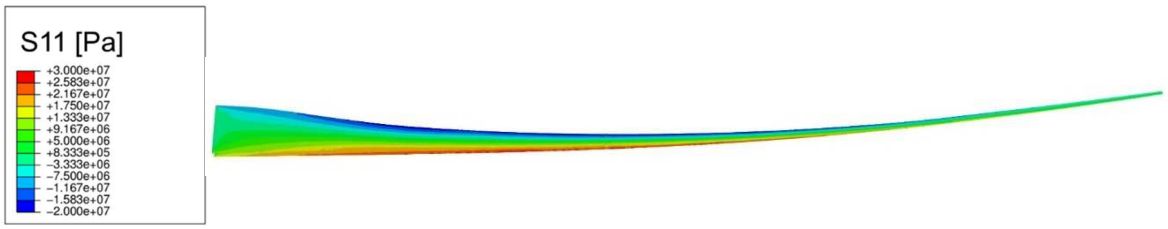

Figure 14: Longitudinal stresses in the shear webs at $+90\ deg$ azimuth angle (FSIg case)

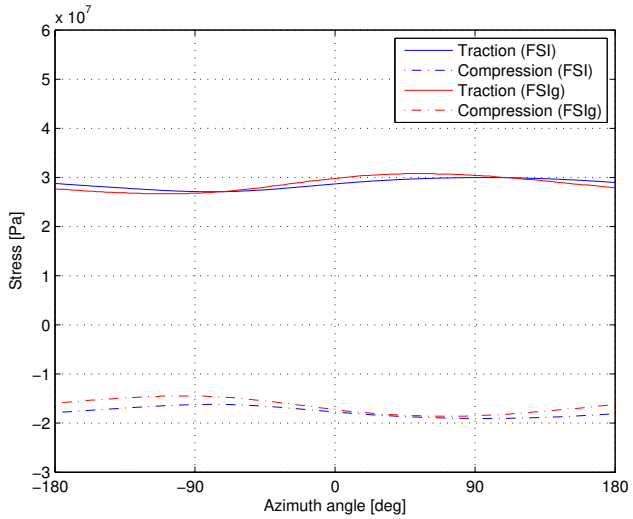

Figure 15: Stress evolution in the maximal traction and compression points of the shear webs.

4 CONCLUSIONS

A coupled FSI model was employed to investigate the effect of the gravity load on the structural response of the composite blades of a large HAWT. The gravity has a clear effect on the bending solicitation acting on the blades and sensibly modifies their deformation both in axial and tangential directions. However, the overall performance level of the machine is not affected by the gravity load: changes in the peak positions of the torque are monitored with a negligible effect on the global performance level of each blade.

REFERENCES

[1] M. Caduff, M.A.J. Huijbregts, H.J. Althaus, A. Koehler, S. Hellweg. Wind power electricity: the bigger the turbine, the greener the electricity? Environmental Science & Technology 2012. DOI: 10.1021/es204108n

[2] Y. Bazilevs, M.C. Hsu, I. Akkerman, S. Wright, K. Takizawa, B. Henicke, T. Spielman, T.E. Tezduyar. 3D simulation of wind turbine rotors at full scale. Part I: Geometry modeling and Aerodynamics. International journal for numerical methods in fluids 2010. DOI: 10.1002/fld.2400

[3] Y. Bazilevs, M.C. Hsu, I. Akkerman, S. Wright, K. Takizawa, B. Henicke, T. Spielman, T.E. Tezduyar. 3D simulation of wind turbine rotors at full scale. Part II: Fluid–structure interaction modeling with composite blades. International journal for numerical methods in fluids 2010. DOI: 10.1002/fld.2400

[4] E. Hau. "Wind Turbines: fundamentals, Technologies, Application, Economics" (2nd Edition). Springer: Berlin, 2006

[5] P.J. Richards, R.P. Hoxey. Appropriate boundary conditions for computational wind engineering models using the k-ε turbulence model. Journal of Wind Engineering and Industrial Aerodynamics 1993, 46 & 47, 145-153.

[6] A. Parente, C. Gorlé, J. van Beeck, C. Benocci. A Comprehensive Modelling Approach for the Neutral Atmospheric Boundary Layer: Consistent Inflow Conditions, Wall Function and Turbulence Model. Boundary Layer Meteorology 2011. DOI 10.1007/s10546-011-9621-5

[7] M. Peeters , W. Van Paepegem. "Development of automated high fidelity finite element models for large wind turbine blades". 16th European Conference on Composite Materials, Seville, Spain, 22-26 June 2014

[8] YJ Lee, YT Jhan, CH Chung. Fluid–structure interaction of FRP wind turbine blades under aerodynamic effect. Composites Part B: Engineering 2012. ISSN 1359-8368

[9] J. Degroote. Partitioned simulation of fluid-structure interaction: Coupling black-box solvers with quasi-Newton techniques. Archives of Computational Methods in Engineering, 20(3):185–238, 2013. DOI: 10.1007/s11831-013-9085-5